This is a repository copy of *Kinetic modelling of dissolution dynamic nuclear polarisation 13C magnetic resonance spectroscopy data for analysis of pyruvate delivery and fate in tumours*.

White Rose Research Online URL for this paper:
https://eprints.whiterose.ac.uk/181205/

Version: Published Version

Article:

RESEARCH ARTICLE

Kinetic modelling of dissolution dynamic nuclear polarisation ^{13}C magnetic resonance spectroscopy data for analysis of pyruvate delivery and fate in tumours

Steven Reynolds[1] | Samira M. Kazan[2] | Adriana Anton[1] |
Tooba Alizadeh[2] | Roger N. Gunn[3] | Martyn N. Paley[1] | Gillian M. Tozer[2] |
Vincent J. Cunningham[†]

[1]Academic Unit of Radiology, Department of Infection, Immunity and Cardiovascular Disease, The Medical School, University of Sheffield, Sheffield, UK

[2]Department of Oncology and Metabolism, The Medical School, University of Sheffield, Sheffield, UK

[3]Department of Brain Sciences, Imperial College London, London, UK

Correspondence
Gillian M. Tozer, Department of Oncology and Metabolism, The Medical School, University of Sheffield, Beech Hill Road, Sheffield, S10 2RX, UK.
Email: g.tozer@sheffield.ac.uk

Funding information
Cancer Research UK; Engineering and Physical Sciences Research Council, Grant/Award Number: C1276/A10345; Medical Research Council; Department of Health (England); University of Sheffield

Dissolution dynamic nuclear polarisation (dDNP) of ^{13}C-labelled pyruvate in magnetic resonance spectroscopy/imaging (MRS/MRSI) has the potential for monitoring tumour progression and treatment response. Pyruvate delivery, its metabolism to lactate and efflux were investigated in rat P22 sarcomas following simultaneous intravenous administration of hyperpolarised ^{13}C-labelled pyruvate ($^{13}C_1$-pyruvate) and urea (^{13}C-urea), a nonmetabolised marker. A general mathematical model of pyruvate-lactate exchange, incorporating an arterial input function (AIF), enabled the losses of pyruvate and lactate from tumour to be estimated, in addition to the clearance rate of pyruvate signal from blood into tumour, K_{ip}, and the forward and reverse fractional rate constants for pyruvate-lactate signal exchange, k_{pl} and k_{lp}. An analogous model

------

was developed for urea, enabling estimation of urea tumour losses and the blood clearance parameter, K_{iu}. A spectral fitting procedure to blood time-course data proved superior to assuming a gamma-variate form for the AIFs. Mean arterial blood pressure marginally correlated with clearance rates. K_{iu} equalled K_{ip}, indicating equivalent permeability of the tumour vasculature to urea and pyruvate. Fractional loss rate constants due to effluxes of pyruvate, lactate and urea from tumour tissue into blood (k_{po}, k_{lo} and k_{uo}, respectively) indicated that T_1s and the average flip angle, θ, obtained from arterial blood were poor surrogates for these parameters in tumour tissue. A precursor-product model, using the tumour pyruvate signal time-course as the input for the corresponding lactate signal time-course, was modified to account for the observed delay between them. The corresponding fractional rate constant, k_{avail}, most likely reflected heterogeneous tumour microcirculation. Loss parameters, estimated from this model with different TRs, provided a lower limit on the estimates of tumour T_1 for lactate and urea. The results do not support use of hyperpolarised urea for providing information on the tumour microcirculation over and above what can be obtained from pyruvate alone. The results also highlight the need for rigorous processes controlling signal quantitation, if absolute estimations of biological parameters are required.

KEYWORDS

dynamic nuclear polarisation, mathematical modelling, P22 rat sarcoma, precursor-product, pyruvate metabolism, rate constant, tumour microcirculation, urea

1 | INTRODUCTION

Dissolution dynamic nuclear polarisation (dDNP) can vastly increase the magnetic resonance spectroscopy (MRS) sensitivity for ^{13}C nuclei, allowing real-time measurement of metabolic kinetics, without the interfering background signals experienced in ^1H MRS.[1,2] $^{13}C_1$-labelled pyruvate ($^{13}C_1$-pyruvate) is the most commonly used substrate in hyperpolarised MRS and imaging (MRI) studies, being the end product of glycolysis and undergoing a number of anabolic and catabolic transformations in energy metabolism. For cancer studies, two important metabolic pathways for pyruvate are the formation of lactate via lactate dehydrogenase, or acetyl-CoA prior to entry into the tricarboxylic acid (TCA) cycle. Pyruvate to lactate exchange in tumours has been studied as a potential marker for the efficacy of anticancer drugs in preclinical studies.[3] More recently, the use of hyperpolarised pyruvate in MRI has been investigated in several clinical studies of prostate, brain and breast cancers.[4–6] Hyperpolarised ^{13}C-labelled urea (^{13}C-urea), which is not metabolised in tissue, except in gut flora, has also been used as a perfusion marker in tumours.[7]

For use in routine clinical work, semiquantitative parameters describing pyruvate to lactate exchange, such as the lactate-to-pyruvate signal ratio, are being evaluated for diagnostic and therapeutic applications.[6] Clinical applications require these parameters to be straightforward and rapidly obtained without the need for expert mathematical input. However, there is also a need for robust quantitation of k_{pl}*, the fractional rate constant for pyruvate signal conversion to lactate, and other related parameters from the ^{13}C spectroscopic data, in order to validate simplified biomarkers[8] and contribute to an understanding of the complex biochemistry of the tumour microenvironment, in which lactate plays a crucial role in energy production, metastasis and immune suppression.[9,10] Preclinical animal systems can make a significant contribution to this field. Bankson et al.[11] found that a simple parameter describing the normalised lactate signal as a fraction of the sum of pyruvate and lactate signals was significantly biased by pyruvate delivery. Such information is important to aid interpretation of similar parameters accessible in clinical studies.

Mathematical models are required to extract kinetic parameters from dDNP data. Previously, we developed a general model of pyruvate to lactate exchange, incorporating an arterial input function (AIF) acquired from measurements in sampled arterial blood, to investigate pyruvate delivery in addition to its metabolism.[12] For the current study, the general model was further developed to provide not only estimates of k_{pl} and the clearance of pyruvate signal from blood into the tissue, K_{ip}, but also the losses of pyruvate and lactate signals from the tissue arising from both physical signal erosion and biological processes. K_{ip} is of particular relevance, due to the influence of pyruvate delivery on semiquantitative measures of pyruvate metabolism[11] and where blood flow effects of treatments are important to understand. Estimates of k_{lo}, the specific

fractional rate constant for the loss of lactate signal from tumour tissue into the blood circulation, is relevant to understanding the high concentration of lactate observed in systemic blood of tumour-bearing subjects.[13,14] An analogous general model was developed to describe the fate of urea in tumour tissue. Previously, we also introduced the precursor-product model for hyperpolarisation studies, which uses the measured tumour pyruvate signal as input for the lactate signal, in order to calculate k_{pl}.[12] A similar 'arterial input-less' model was also developed by Khegai et al.[15] and adopted by Larson et al.[16] For the current study, the precursor-product model was further developed to account for an observed delay between the appearance of the lactate and pyruvate signals in tumour tissue following administration of hyperpolarised pyruvate and to enable estimation of total lactate losses from tumour tissue.

The main aim of the current study was to use the general models to carry out a comprehensive analysis of the fate of exogenously administered hyperpolarised pyruvate and urea in a rat tumour model. Thus, delivery parameters for pyruvate and urea, defined as the clearance rates of hyperpolarised pyruvate and urea signals from arterial blood into tumour tissue (K_{ip} and K_{iu}, respectively), the forward and reverse fractional rate constants for pyruvate-lactate signal exchange (k_{pl} and k_{lp}, respectively) and the fractional loss rate constants for hyperpolarised pyruvate, lactate and urea signals due to efflux from tumour into blood (k_{po}, k_{lo} and k_{uo}, respectively) were estimated. The influence of arterial blood pressure, as a principal determinant of tumour blood flow in experimental tumours,[17–19] on K_{ip} and K_{iu}, was investigated. We hypothesised that hyperpolarised pyruvate provides the same information on the permeability of the tumour vasculature as hyperpolarised urea, due to efficient carrier systems in each case. The results confirmed that the use of urea in hyperpolarisation experiments did not provide any information on the tumour microcirculation over and above what could be obtained from pyruvate alone. A second aim was to interrogate the modified precursor-product model to investigate the kinetics of the delayed lactate signal in tumour tissue and the total lactate signal losses from tumour tissue arising from metabolism, efflux into blood and signal loss, in addition to estimating k_{pl}. Incorporation of a tumour 'waiting room' compartment into the model, in which pyruvate was unavailable for metabolism (described by k_{avail}), enabled more accurate estimates of k_{pl}, with k_{avail} likely reflecting the degree of functional tumour vascularisation. Estimating total lactate losses from tumour tissue at different scanning repetition times (TRs) enabled calculation of the average flip angle (θ) and lower limits on the longitudinal relaxation times for pyruvate and urea (T_{1p} and T_{1u}, respectively) in tumour tissue.

2 | METHODS

2.1 | Animal preparation

Animal experiments were conducted in accordance with the United Kingdom Animals (Scientific Procedures) Act 1986, with local ethical approval and following published guidelines for the use of animals in cancer research.[20] In-house bred adult male BDIX rats (originally supplied by Charles River UK Ltd, Margate, UK) were used for these experiments. Breeding was carried out under barrier conditions, but the health status of the animals used was not specifically tested. Using an aseptic technique under general anaesthesia, rats were subcutaneously implanted in the rear dorsum with fragments of the rat P22 sarcoma,[12] a tumour originating in our laboratory and used here at early passage generations.[19] After several weeks, when tumours reached a mean diameter of approximately 15 mm, the animals were transferred to a dedicated animal scanner facility and prepared for MRS, as described previously.[12] Briefly, animals were anaesthetised with isoflurane (5% induction; 1.5%–2% maintenance in 1:1 O_2:N_2O at 2 L/min). Rectal temperature was monitored and maintained at ∼37°C throughout surgical procedures using a homoeothermic blanket (Harvard Apparatus, UK) and an overhead lamp. Two blood vessels were cannulated: a femoral vein for delivery of the hyperpolarised materials and a femoral artery for blood pressure monitoring and AIF, T_1 and θ estimations (see below). Cannulas were primed for surgery with heparinised saline and rats were heparinised postsurgery with 0.1 ml of 1000 units per ml heparin by intravenous bolus injection via the cannulated femoral vein.

2.2 | Preparatory MR methods

Following surgery, the animals were transferred to a dedicated animal holder for scanning, where the arterial cannula was connected to a chamber for arterial blood collection and the venous cannula was connected to an automated injection system (Figure 1A,B). The arterial blood-collecting chamber was connected to a custom-made pump for arterial blood withdrawal, operated as previously described.[12] The chamber itself was of similar design to that previously described,[12] with the addition of a fibre optic temperature probe (PalmSense AMS Technologies AG, Martinstried, Germany) glued inside the chamber to measure the temperature of the withdrawn blood (Figure 1B). The cannula dead-space to the chamber was ∼100 μL and the total chamber volume was 275 μL.

The holder was then positioned at the centre of a Bruker 7-T, 300-mm bore animal magnet system, initially consisting of an Avance II scanner with a 400-mT/m, 120-mm diameter gradient insert, and subsequently an Avance III scanner with a 660-mT/m, 120-mm gradient insert. Identical MR sequence acquisition parameters and the same RF coil were used on both systems to minimise any intersystem differences. Anaesthesia was maintained using isoflurane and medical air at 2 L/min via a nose cone, and the body temperature continued to be maintained in the scanner using
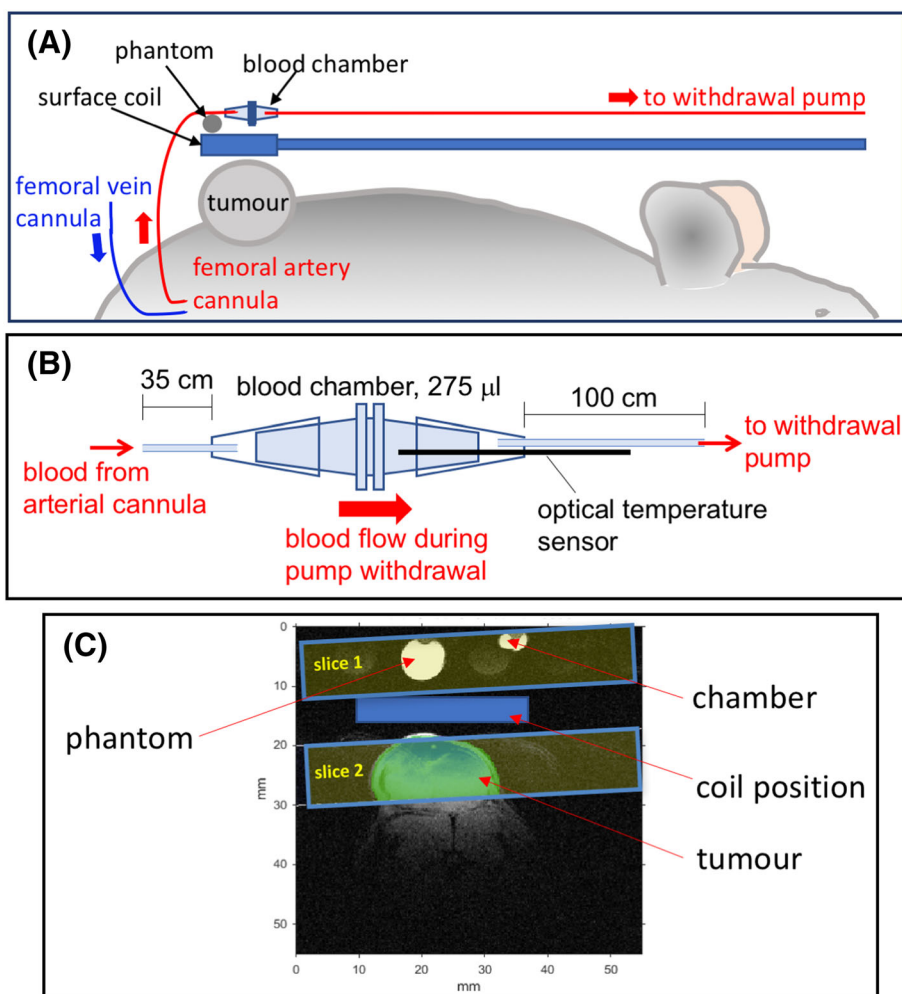
FIGURE 1 Experimental setup for arterial blood sampling and blood/tumour MRS; not to scale. (A) Approximate positions of subcutaneous tumour on the rat, surface coil, phantom and blood chamber; the blue arrow shows the direction of administration for hyperpolarised pyruvate and urea; the red arrow shows the direction of arterial blood flow. (B) Details of the blood chamber and connecting cannulas. (C) An example FLASH image of a tumour, including the phantom and chamber and the approximate positions of the surface coil and slices 1 and 2, with the green/blue shading indicating the tumour volume within slice 2

a thermostatically controlled heating blanket and warmed air. A 20-mm ^{13}C/^{1}H tuned surface coil for transmission and receiving signal (Bruker Biospin MRI GmbH, Ettlingen, Germany) was supported 1–2 mm above the tumour (to avoid artefacts due to animal movement during respiration). A 6.7 M sodium ^{13}C$_1$-acetate phantom was placed in the same location on the surface coil for all experiments to provide a reference signal and the arterial blood-collecting chamber was positioned next to the phantom, as shown in Figure 1A,C. Structural images were acquired using a fast low-angle shot (FLASH) sequence with field of view (FOV) = 6 × 6 cm, matrix size 512 × 512, $\theta = 30°$, TR = 114 ms, echo time (TE) = 6 ms and NEX = 1. Tumour structural images were used to estimate tumour volumes selected for MRS.

2.3 | Hyperpolarisation experiments with ^{13}C$_1$-pyruvate and ^{13}C-urea

For the hyperpolarised MR experiments, two samples were prepared: (i) ^{13}C$_1$-pyruvic acid (PA) and (ii) 12 M ^{13}C-urea dissolved in $\sim$3:2 ^{12}C-DMSO:D$_2$O, both containing 15 mM OXO63 trityl radical (Oxford Instruments, Abingdon, UK). Next, 1.5 mM DOTAREM (Guerbet, Roissy, France) was added to each sample to enhance the final polarisation level; 45.5 ± 0.5 mg ($\sim$35 μL) of the PA sample was flash-frozen in a sample cup using liquid nitrogen, after which 35 μL of the urea sample was frozen on top. The dual frozen sample was inserted into a HyperSense (Oxford Instruments) dDNP system and polarised for $\sim$2 hours. The polarisation of PA alone took less than 1 h. Following acquisition of a FLASH image, as described above, the hyperpolarised frozen sample was dissolved with superheated 40 mM HEPES buffer solution and transferred under pressure to the custom-designed automated injection system[21] connected to the femoral vein cannula (Figure 1A), ready for rapid injection into the rat. The receiving vessel also contained a predetermined aliquot of 2.0 M sodium hydroxide solution required to neutralise the PA acidity.

The final concentrations of PA and urea were 150 and 121 mM, respectively (PA animal dose ~0.75 mmol/kg). Following hyperpolarisation of PA and urea, the dissolution transfer time from the polariser to the receiving vessel was 6 s, at which time the injection procedure was triggered (t = 0), whereby 5 ml/kg of the solution containing hyperpolarised substrate was automatically injected through the femoral vein cannula, over a period of 13 s; the automated injector provided a reproducible delivery profile.[21] MRS data acquisition began at t = 0 for experiment 1 and t = 40 s for experiments 2 and 3 (see below).

One-dimensional MRS ^{13}C spectra were collected using a 0.5-ms Gaussian RF pulse, with 8-mm slice selection and a nominal θ of 20° for a slice incorporating the arterial blood-collecting chamber and the phantom (slice 1) and a slice-incorporating tumour tissue (slice 2) (Figure 1C). Slice-localised free induction decay signals (256 points, 50 ppm sweep width) were acquired with a different TR depending on the experiment performed, as described below. Approximately 10 min after injection, the femoral cannula was flushed through with 0.5 ml of heparinised saline. The above procedure was carried out three sequential times in each animal, except that only PA was hyperpolarised and administered in the third run (experiment 3). The individual experiments are summarised in Figure 2A and described in detail below.

In experiment 1, 1.0 ml of arterial blood was withdrawn at a rate of 1.0 ml/min, during which time the hyperpolarised signal was continuously acquired using TR = 1 s, to provide data for simultaneously estimating the AIFs for pyruvate and urea.

In experiment 2, arterial blood was withdrawn at 1.0 ml/min to completely fill the chamber and then held stationary, with signal acquired from t = 40 s, using TR = 4 s.

In experiment 3, arterial blood was withdrawn and signal acquired as in experiment 2, except using TR = 0.211 s for rapid signal erosion from the applied RF pulses.

Experiments were carried out in the same order for each animal. Signal time-courses from the chamber in experiments 2 and 3 provided data for estimating T_{1p} and T_{1u} in arterial blood and the average RF flip angle (θ) transmitted by the surface coil. For each of these injections, simultaneous signals were also acquired from slice 2 containing tumour tissue (Figure 1C).

Throughout the scanning procedures, arterial blood pressure and respiration rate were monitored continuously using an in-line pressure transducer (CWE Inc., Ardmore, PA) and surface pressure transducer (SA Instruments Inc., Stony Brook, NY), respectively, in order to assess the physiological state of the animals. Mean arterial blood pressure (MABP) measurements during experiment 1 were also used to determine their influence on delivery of hyperpolarised pyruvate and urea to tumour tissue (K_{ip} and K_{iu}, respectively). Approximately 3 min after each hyperpolarised substrate injection and data acquisition, an arterial blood sample was taken to determine blood pO_2, pCO_2 and pH (ABL80/800 Flex blood gas analyser, Radiometer Ltd, Crawley, UK). At the end of the procedures, animals were sacrificed via an intravenous overdose of sodium pentobarbitone.

2.4 | Obtaining a signal time-course

Data were processed using custom Matlab software (MathWorks, Natick, MA) to provide magnitude spectra for chamber blood (slice 1) and tumour tissue (slice 2). In a development from our previous study,[12] MR spectral baselines were corrected by selecting baseline points on an averaged spectrum from the time-course. From the defined baseline points, interpolated baseline corrections (Savitzky Golay filtered) were then created and applied to each time-course spectrum. The resulting spectra were integrated (Matlab trapz function) to produce a signal time-course for each spectral component ($^{13}C_1$-pyruvate, $^{13}C_1$-lactate, ^{13}C-urea). Any remaining small nonzero offsets in the signal time-courses were accounted for by fitting for an offset term (not explicitly shown in the equations below), in initial analyses of each dataset. The fitted offsets were then carried through as fixed values, so that the same offset was used in obtaining parameter estimates from different mathematical models applied to an individual dataset. Due to complexities in quantitation of ^{13}C spectra and uncertainties, for instance in polarisation level and B1 homogeneity, the kinetic parameters described below should be considered apparent rate constants.[15]

2.5 | Flip angle and T_1 estimates from arterial blood

T_{1p} and T_{1u} were estimated in blood for subsequent application in tumour modelling, as reported by others.[22,23] Use of blood minimises the effects of metabolism, which are difficult to eliminate in solid tissues. Our online method means that T_1 was determined with minimal delay and degradation of the blood sample and holding the blood stationary eliminated signal losses from blood flow. The equation used to estimate T_1 relaxation effects depends on both T_1 and the applied flip angle (θ):

$$M(t,n) = M_0 \, (cos\theta)^n \, e^{-\frac{nTR}{T1}},$$ (1)

where $M(t, n)$ is the decaying magnetisation as a function of TR and the nth pulse/data acquisition, and M_o is the initial magnetisation. The non-uniform B1 profile of the surface coil results in a reduced θ (from the original set value of 20°) as a function of distance. Equation 1 was solved

(A)	Experiment 1		Experiment 2	Experiment 3
^{13}C-labelled compound	pyruvate urea		pyruvate urea	pyruvate
TR (s)	1		4	0.211
estimates from blood	AIFs		T_{1p}, T_{1u}, θ	
mathematical model for tumour analysis	General	Precursor-Product (+ waiting room)	Precursor-Product	Precursor-Product
tumour estimates	k_{pl}, k_{lp}, K_{ip}, R_p, R_l K_{iu}, R_u	k_{pl}, $k_{loss(lactate)}$ (+ k_{avail})	k_{pl}, $k_{loss(lactate)}$	k_{pl}, $k_{loss(lactate)}$
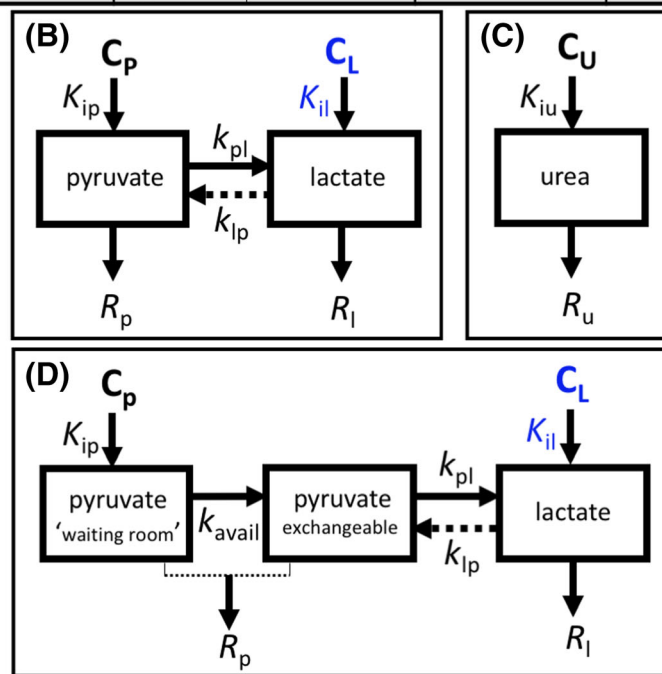
FIGURE 2 Summaries of (A) The three experiments carried out sequentially in each rat and (B-D) The different models used for parameter estimation. TR is the scan repetition time; AIF is the arterial input function as 'seen' by tumour tissue; T_{1p} and T_{1u} are the estimated longitudinal relaxation times for hyperpolarised pyruvate and urea, respectively, in blood; θ is the estimated average flip angle; R_p and R_l are estimated lumped fractional rate constants comprising tumour losses from T_1s, θ and efflux into blood (k_{po} and k_{lo}) for pyruvate and lactate, respectively, as defined in Equations 4 and 5 in the main text; R_u is the equivalent parameter for urea (Equation 7); tumour k_{pl} and k_{lp} are the forward and reverse fractional rate constants for pyruvate-lactate signal exchange, respectively; k_{avail} is the fractional rate constant for transfer of pyruvate signal from the nonexchanging to the exchangeable tumour compartment in the 'waiting room' model in (C); $k_{loss(lactate)}$ is the fractional rate constant for total loss of lactate signal from tumour $= R_l + k_{lp}$; K_{ip} and K_{iu} are the clearance rates from arterial blood into tumour tissue for pyruvate and urea, respectively; C_P and C_U are the respective AIFs. K_{il} and C_L are the equivalent parameters for lactate, shown in blue to denote that they were not included in the model equations because no lactate signal was detected in arterial blood

simultaneously for T_{1p}, T_{1u} and θ using data from experiment 2 (TR = 4 s) and experiment 3 (TR = 0.211 s) (see Appendix A). It was assumed that T_1 for lactate (T_{1l}) = T_{1p} and that θ derived from pyruvate data could also be applied to urea data.

2.6 | Obtaining an AIF

The experimentally measured signal time-course from arterial blood passing through the chamber differs from the actual AIF experienced by the tumour because of delay and dispersion of the signal between the chamber and the tumour, and relaxation losses due to T_1 and RF pulses in the

chamber. The deconvolution of these effects from the measured signal time-course in the chamber blood has been described previously,[12] assuming that blood in the chamber is well mixed and a gamma-variate function describes the AIF, with an exponential term describing dispersion in the measuring chamber. Fits of signal time-courses from experiment 1 using this method were compared with those obtained from a 'spectral' fitting method,[24] in which a sum of exponential basis functions is convolved with a square wave input (representing the infusion schedule) to derive the AIF. This method has the advantage of making minimal assumptions about the shape of the AIF or its arrival time (see Appendix B). The AIFs obtained from the spectral fitting method were then used in all the estimations of the tumour parameters derived from the general models summarised in Figure 2.

2.7 | Estimation of kinetic parameters in tumours: general models

Following intravenous injection of PA, $^{13}C_1$-lactate and occasionally $^{13}C_1$-alanine are observed in tumours. The focus of the present work was on the kinetic exchange between $^{13}C_1$-pyruvate and $^{13}C_1$-lactate. The general models used to describe the fate of pyruvate and urea in tumour tissue are illustrated as compartments in Figure 2B-D. Pyruvate metabolism is described as a two-way exchange model for metabolic conversion between $^{13}C_1$-pyruvate and $^{13}C_1$-lactate (Figure 2B). In the absence of any measurable signal from hyperpolarised lactate in arterial blood, this is presented in the form of two differential equations, as described previously[12]:

$$\frac{d\mathbf{PP}}{dt} = -\left(R_p + k_{pl}\right)\mathbf{PP}(t) + k_{lp}\mathbf{LP}(t) + K_{ip}\mathbf{C_P}(t) \tag{2}$$

$$\frac{d\mathbf{LP}}{dt} = k_{pl}\mathbf{PP}(t) - \left(R_l + k_{lp}\right)\mathbf{LP}(t), \tag{3}$$

where $\mathbf{PP}(t)$ and $\mathbf{LP}(t)$ are the pyruvate and lactate signals (arbitrary units per ml tumour tissue), respectively, deriving from the pyruvate AIF, $\mathbf{C_P}(t)$ (arbitrary units per ml arterial blood). All tumour signals were normalised to tumour volume in slice 2, calculated from the FLASH images (signal per ml tumour), enabling estimation of K_{ip} in millilitres of blood cleared per min per millilitre tumour tissue (ml.min^{-1}.ml^{-1}). Because the volumes of the different tumour compartments (Figure 2) are unknown, all other parameter estimates are fractional rate constants and independent of tumour volume. k_{pl} (s^{-1}) and k_{lp} (s^{-1}) are, respectively, the fractional forward and reverse rate constants for pyruvate-lactate signal exchange in tumour tissue. R_p and R_l are lumped parameters incorporating the other main losses of pyruvate and lactate signals, respectively, from tumour tissue and defined by:

$$R_p = \frac{1}{T_{1p}} + \frac{[1 - \cos(\theta)]}{TR} + k_{po} \tag{4}$$

and

$$R_l = \frac{1}{T_{1l}} + \frac{[1 - \cos(\theta)]}{TR} + k_{lo}, \tag{5}$$

where k_{po} (s^{-1}) and k_{lo} (s^{-1}) are the fractional loss rate constants for pyruvate and lactate signals due to efflux from tumour into blood, respectively, and T_1s/θ were derived from arterial blood. Detailed solutions of Equations 2 and 3 are given in Kazan et al.[12]

The general model used to describe the fate of urea in tumour tissue (Figure 2C) is similarly described by the following equations:

$$\frac{d\mathbf{UU}}{dt} = -\left(R_u\right)\mathbf{UU}(t) + K_{iu}\mathbf{C_u}(t) \tag{6}$$

and

$$R_u = \frac{1}{T_{1u}} + \frac{[1 - \cos(\theta)]}{TR} + k_{uo}, \tag{7}$$

where $\mathbf{UU}(t)$ is the urea signal in the tumour deriving from the direct urea input function $\mathbf{C_u}(t)$; K_{iu} has the units ml.min^{-1}.ml^{-1}, as described above for the equivalent pyruvate parameter; R_u is the lumped loss parameter; and k_{uo} is the fractional loss rate constant for urea signal due to

efflux from tumour into blood. Because urea is not metabolised in tumour tissue, there are no losses equivalent to k_{pl} and k_{lp}. The solution to Equation 6 is given by:

$$\mathbf{UU}(t) = \mathbf{C_U}(t) \bigotimes K_{iu} \exp(-R_u t). \tag{8}$$

All analyses were carried out in Matlab (version R2016b). The tumour tissue signal time-courses were fitted to the general models shown in Figure 2B,C using a nonlinear optimiser (Nelder Mead[25]) that incorporated fixed values for the signal arrival times, in order to obtain the least squares fit and extract the required parameter estimates (Figure 2). The signal arrival times were estimated from prior fits to the initial part of the pyruvate and lactate signal time-courses. Using the general model for pyruvate-lactate conversion, as described above, the following tumour parameters were estimated using the AIF and the tumour signal time-courses in experiment 1: K_{ip}, k_{pl}, k_{lp}, R_p, R_l; where $(R_p + k_{pl})$ and $(R_l + k_{lp})$ represent the fractional rate constants for total loss of pyruvate and lactate signals from tumour tissue, $k_{loss(pyruvate)}$ and $k_{loss(lactate)}$, respectively:

$$k_{loss(pyruvate)} = R_p + k_{pl} = \frac{1}{T_{1p}} + \frac{[1 - \cos(\theta)]}{TR} + k_{po} + k_{pl} \tag{9}$$

$$k_{loss(lactate)} = R_1 + k_{lp} = \frac{1}{T_{1l}} + \frac{[1 - \cos(\theta)]}{TR} + k_{lo} + k_{lp}. \tag{10}$$

Corresponding parameter estimates obtained for urea were K_{iu} and R_u.

2.8 | Estimation of kinetic parameters in tumours: precursor-product models

Previously[12] and in the current study, we detected no lactate signal in the blood chamber during PA infusion, such that there was no observable arterial delivery of hyperpolarised lactate to the tumour ($K_{il} = 0$). Under these conditions, hyperpolarised pyruvate in the tumour is the only source of hyperpolarised lactate in the tumour. Therefore, a precursor-product model, in which the tumour pyruvate signal was used as the input for lactate, was used to provide estimates of k_{pl} and $k_{loss(lactate)}$ from experiments 1, 2 and 3 (Figure 2 and Appendix C). In a development from our previous study,[12] the raw pyruvate signal per ml tumour time-course was used as the input for the lactate data. The nonlinear optimiser (Nelder Mead[25]) was used to obtain the least squares solution and extract estimates of k_{pl} and $k_{loss(lactate)}$. Estimates of $k_{loss(lactate)}$ from experiments 1 and 2 were used to solve for tumour tissue θ, using Equation 10 and assuming that T_{1l}, k_{lo} and k_{lp} remained constant between experiments. A lower limit estimate of T_{1l} in tumour tissue was then estimated by substituting these tumour estimates of θ and estimates of R_l into Equation 5, with k_{lo} set to 0. Similarly, using Equation 7, a lower limit estimate of T_{1u} in tumour tissue was calculated (with k_{uo} set to 0).

Delays of a few seconds were routinely observed between the arrival times of the tumour pyruvate and lactate signals. In the standard precursor-product model and the general model, the time delays were estimated then incorporated into the fits as fixed values. In the final model used, the precursor-product model was modified to include an extra compartment to account for the delayed arrival time of the lactate signal. This extra 'waiting room' compartment was described by a fractional rate constant denoted as k_{avail} (s^{-1}), estimated in addition to k_{pl} and $k_{loss(lactate)}$ (Figure 2D). The least squares solution was again obtained using the Nelder Mead optimisation algorithm. Further details of the precursor-product models and delays are provided in Appendix C.

All the mathematical models used and the tumour parameters estimated are summarised in Figure 2A. The source code for the various models are available upon request.

2.9 | Statistics

Statistical analysis of the kinetic parameter estimates obtained from different modelling procedures was carried out using GraphPad Prism software version 7.0b for Mac OS X (GraphPad Software Inc., San Diego, CA). Two-way paired Student's t-tests were used for statistical comparison of two parameter sets estimated in the same group of animals and a one-way ANOVA with repeated measures, followed by a Tukey post-hoc test, was used for comparison of more than two parameter sets. Datasets were not tested for normal distribution. Linear regression analysis was used for comparing different parameters in individual animals. Values are expressed as mean ± SEM. In all cases, differences between results were described as significant if the probability corresponding to the relevant statistic was less than 0.05.

3 | RESULTS

3.1 | Animals and tumours

A group size of 12 tumour-bearing animals was chosen on the basis of previous estimates of k_{pl}, where the SEM was approximately 6% for nine animals.[12] Some attrition was anticipated due to experimental complexity, but no specific exclusion criteria were set. In practice, one animal was sacrificed prior to experiment 2 due to unacceptable injectate pH, one was sacrificed prior to experiment 2 following blood loss from the cannulation site and, in a third, there was very poor signal-to-noise ratio in the tumour for both experiments 1 and 3, which precluded analysis. Results from these three animals were excluded from the final analyses. The tumour geometrical mean diameter from in vivo caliper measurements in three dimensions for the animals included in the final analyses was 14.7 ± 1.2 mm; the animals weighed 318 ± 13 g (n = 9).

3.2 | Estimates of T_{1p}, T_{1u} and θ in arterial blood

Figure 3 shows an example of the spectra acquired in arterial blood (red) and tumour tissue (blue) for an individual animal. Figure 4A illustrates the signal decays, with associated fits, in the blood chamber for experiments 2 and 3. Figure 4B shows the associated estimates of θ, T_{1p} and T_{1u} from arterial blood for the group as a whole. Mean θ for the slice was estimated as 9.7 ± 0.9 degrees. T_{1p} and T_{1u} were significantly different from each other (16.6 ± 1.2 and 10.4 ± 1.2 s, respectively; $p < 0.0001$). Figure 4C shows that there was no significant effect of blood temperature on estimates of T_1s over the observed temperature range in the chamber ($p = 0.920$ and $p = 0.466$ for the slopes of the fitted lines being nonzero, for pyruvate and urea, respectively). Marjanska et al.[23] estimated the T_1 of pyruvate as 31 ± 1 s in ex vivo rat blood at 9.4 T at room temperature but as 13.2 ± 4.3 s in the carotid artery scanned in vivo, a value much closer to ours. Notably, in our previous study,[12] we used an estimated T_{1p} in
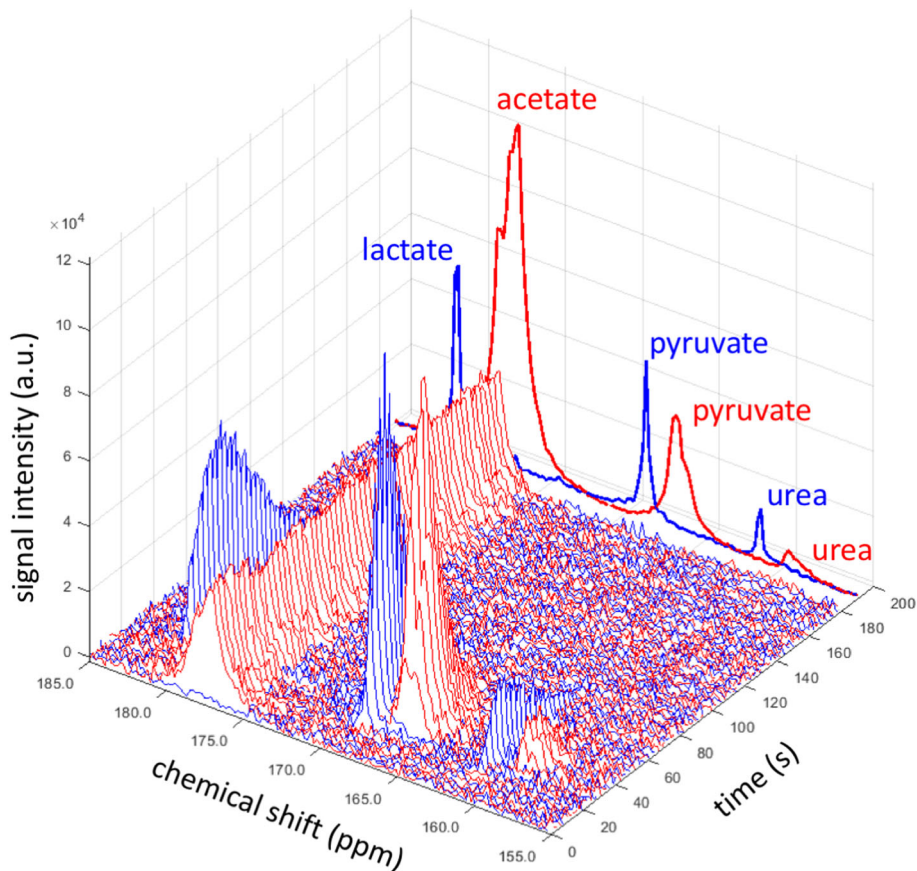
FIGURE 3 Time-course plot of slice-selected ^{13}C spectra obtained from the arterial chamber (red) and tumour tissue (blue) in an individual animal from experiment 1. Acquisition was started (time = 0) after a trigger signal, provided by the HyperSense at the point of dissolution. Every third spectrum in the time-course is shown for clarity. Projected at the rear of the time-course are the mean spectra (rescaled for visibility) for the respective slices showing the detected metabolites. Spectra are referenced to acetate at 177 ppm; the frequency shift in signal between chamber and tumour is due to inhomogeneity in the field
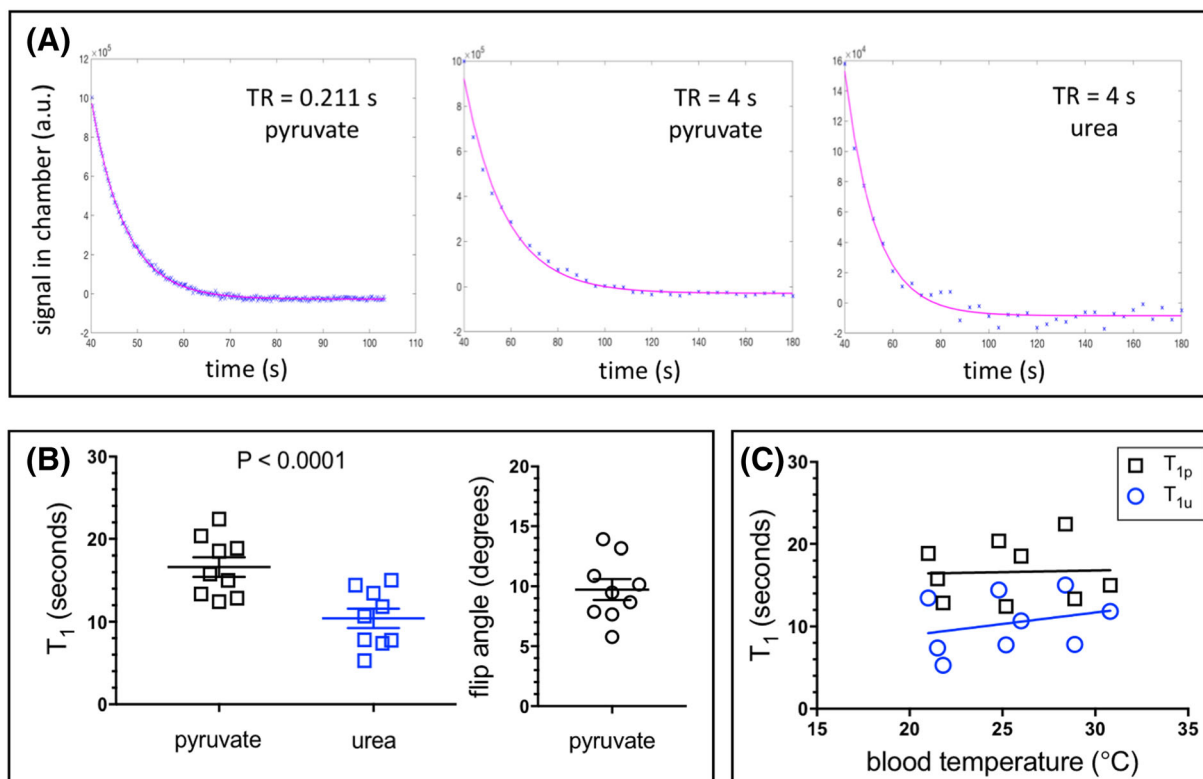
FIGURE 4   Analysis of arterial blood in experiments 2 and 3. (A) Examples of signal time-courses in arbitrary units (a.u.) for pyruvate and urea in arterial blood for experiment 2 (TR = 4 s) and experiment 3 (TR = 0.211 s) in the same individual animal, as shown in Figure 3. Signal acquisition was started 40 s into the infusion time of hyperpolarised compounds to ensure that the blood chamber was filled with arterial blood from the femoral cannula. Data points are shown as blue crosses; magenta lines are fits through the data (as described in Appendix A). (B) Parameter estimates for T_1s for pyruvate and urea and average flip angle; each point represents an individual tumour and bars are means ± SEM for n = 9; p value is from a two-tailed paired t-test. (C) Variation in T_1s with blood temperature; lines are fitted by linear regression analysis and the slopes of the lines are insignificantly different from 0, with $p = 0.920$ and $p = 0.466$ for pyruvate and urea, respectively; n = 9

arterial blood of 43 ± 1 s for use in tumour modelling. However, the previous study estimated combinations of T_1p and θ from a single experiment, rather than using simultaneous equations from different TR periods to provide a discrete estimate of T_{1p}, as done here. The individual arterial blood T_{1p}, T_{1u} and θ estimates for each animal were applied in the analysis of the respective animal's tumour tissue, with no temperature correction made.

3.3 | AIFs and the general models

Figure 5 illustrates the processes for obtaining and using pyruvate and urea AIFs. Visually, the spectral method provided a closer fit to the arterial blood data in the chamber than the gamma-variate (Figure 5A). This was confirmed for the animal group as a whole, where the spectral method yielded residual sum of squares for the fits to the arterial blood data that were 32% ± 7% and 7% ± 3% lower than the gamma-variate fits, for pyruvate and urea, respectively (n = 9 animals). Figure 5B shows the derived AIFs as 'seen' by the tumour following correction for dispersion effects, and also the actual blood signal data points per ml chamber arterial blood. In Figure 5C, fits to the tumour data using the general models (Figure 2B,C) that incorporate AIFs derived from the gamma-variate and spectral methods are shown (red and blue lines, respectively) (refer to the figure legend for further details). Because the spectral analysis method provided the best fits to the blood data, the tumour pyruvate and urea fits derived from the spectral method AIFs were used for the subsequent steps in the general model analysis.

3.4 | Estimates of k_{pl}, k_{lp} and losses using the general models

k_{pl} was estimated as $0.049 ± 0.006$ s^{-1} (n = 9) using the general model (Figure 6A), which is very similar to that obtained previously for the P22 tumour under similar conditions.[12,26] As expected, estimates of k_{lp} from the general model were very low compared with k_{pl} and overall were indistinguishable from zero ($-0.003 ± 0.003$ s^{-1}; Figure 6B).
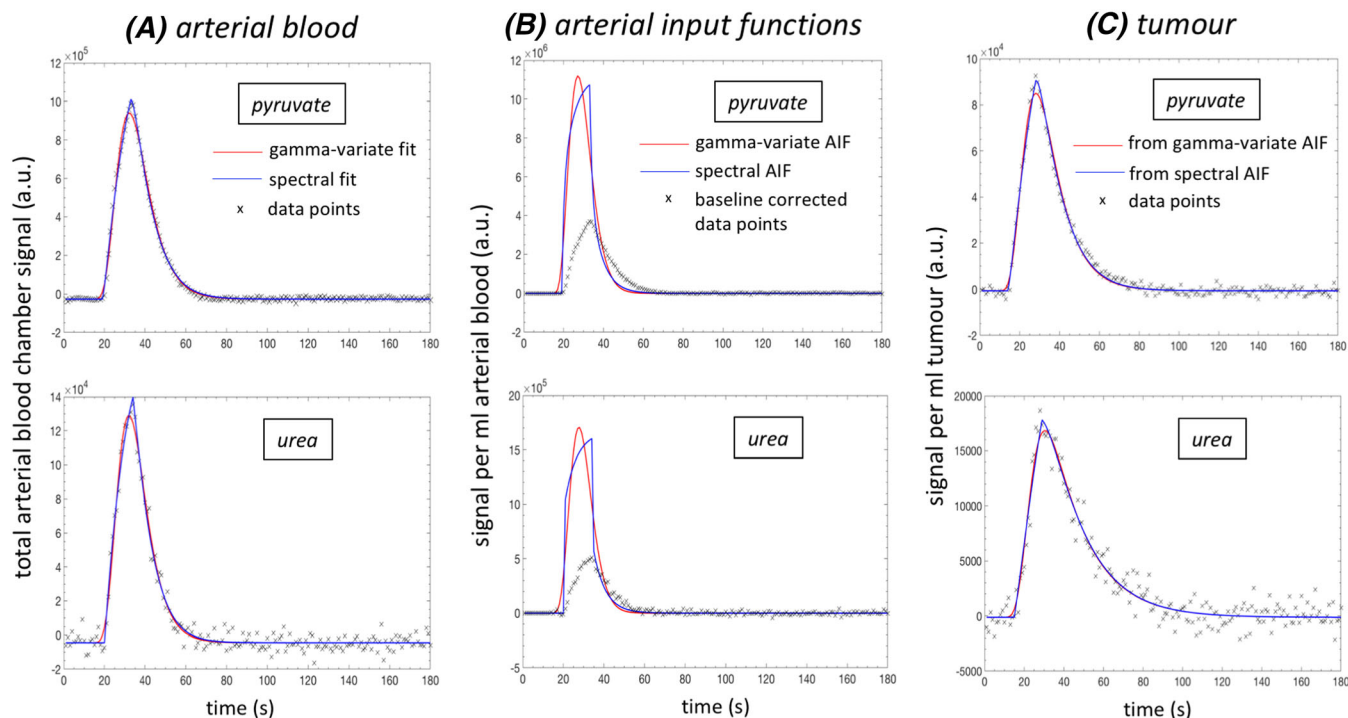
FIGURE 5 Estimation and use of arterial input functions (AIFs) using the general model, in the same individual animal as shown in Figures 3 and 4. (A) Signal time-courses for pyruvate and urea in the arterial blood in the chamber, as blood was withdrawn via the femoral artery in experiment 1 (black crosses); red lines are assuming a gamma-variate shape for the AIF; blue lines are fits from spectral analysis (Appendix B). (B) AIFs for pyruvate and urea (C_P and C_U) derived from the gamma-variate (red) and spectral (blue) fitting procedures and correcting for delay and dispersion in the circulation and signal decay, as described in the main text; black crosses are the raw data with baseline correction. (C) Measured tumour signal time-courses for pyruvate and urea (black crosses) and the fitted data based on the gamma-variate AIF (red line) and spectral AIF (blue line)

The general model for pyruvate-lactate exchange also provided estimates of the parameter R_l, as defined in Equation 5, such that k_{lo} could be calculated. Accurate estimates of k_{lo} would help to describe the fate of lactate in tumour tissue following metabolic perturbation. Figure 6C,D shows the R_l and k_{lo} estimates (0.053 ± 0.008 and -0.025 ± 0.01 s^{-1}, respectively). The most obvious feature of the data is that the k_{lo} estimates are all negative, with the exception of a single outlier attributable to a particularly high estimate of R_l, as seen in Figure 6C. Negative k_{lo} suggests an influx of lactate from blood into tissue. However, if there are discrepancies between T_{1l} and θ in blood versus tumour tissue, these could easily account for the negative values obtained.

The same loss parameters for urea (R_u and k_{uo}, Equation 7) were compared with those for pyruvate (R_p and k_{po}, Equation (4), as shown in Figure 6E,F. A higher blood T_1 for pyruvate than for urea (Figure 4) is consistent with R_u being higher than R_p in tissue (Figure 6E; $p = 0.047$). The fractional rate constants k_{po} and k_{uo} were negative (Figure 6F), as described for lactate (Figure 6D). Assuming that this is due to blood values for T_1s and θ being inaccurate estimates of the corresponding tumour values, any further calculations based on these values are quantitatively meaningless.

3.5 | Estimates of the clearances of pyruvate and urea from blood to tumour tissue using the general model

The blood clearance parameters, K_{ip} and K_{iu}, are dependent on blood flow rate and the permeability of the tissue vasculature to the particular solute, described mathematically by $K_i = E \times F$, where E is the fraction of solute extracted or cleared from the blood on a single pass and F is the blood flow rate in ml blood per min per ml tissue.[27] Therefore, any difference in K_i between pyruvate and urea would denote a difference in permeability of the tumour vasculature to the two solutes, because they were administered simultaneously, ensuring identical blood supply conditions.

Figure 7A shows that there was a highly significant correlation between K_{ip} and K_{iu} in individual animals. Furthermore, K_{ip} and K_{iu} were equivalent (0.149 ± 0.028 and 0.148 ± 0.029 ml.min^{-1}.ml^{-1}, respectively; $p = 0.975$), suggesting that the P22 tumour vasculature is equally permeable to pyruvate and urea.
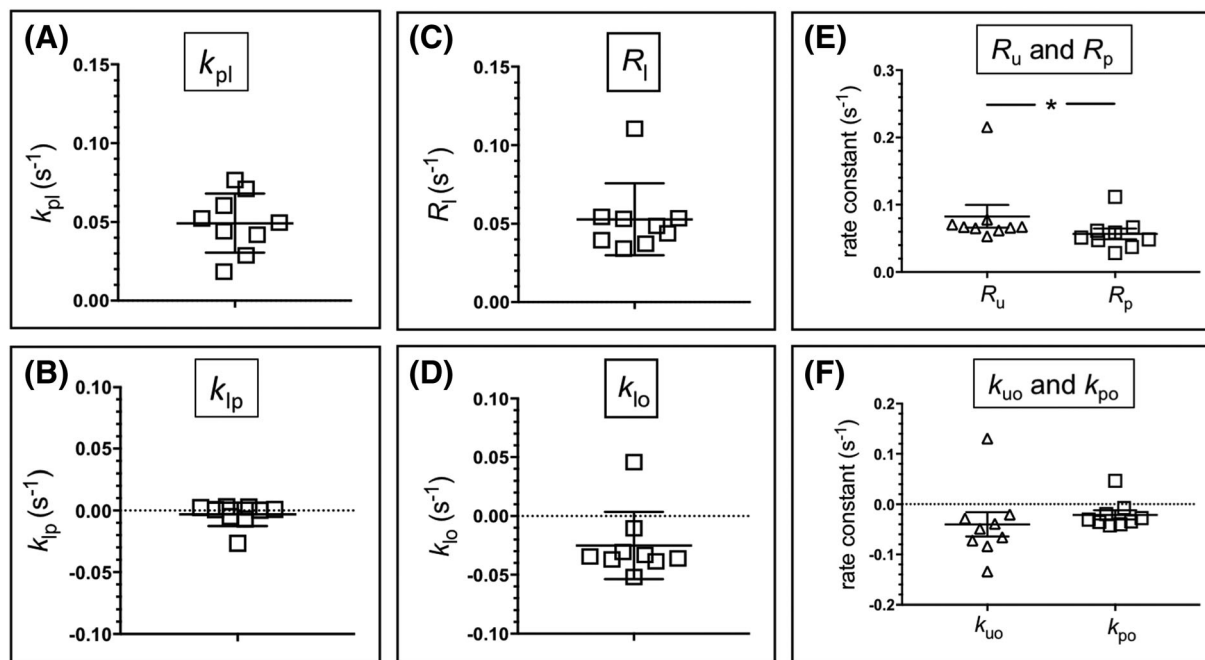
FIGURE 6 Analysis of tumour metabolism and losses using the general model. (A) Estimates of k_{pl}, the fractional rate constant representing pyruvate-lactate metabolism; (B) Estimates of k_{lp}, the fractional rate constant representing reverse metabolism lactate-pyruvate; (C) Estimates of R_l, the fractional rate constant representing the main losses of lactate from tumour tissue, comprising losses from T_{1l}, θ and k_{lo}, as defined in Equation 5 in the main text; (D) Estimates of tumour k_{lo} calculated from Equation 5 in the main text, which uses estimates of T_1s and θ from arterial blood in the chamber, as described in the main text; (E) Estimates of R_u and R_p, the fractional rate constants representing the main losses of urea and pyruvate from tumour tissue, comprising losses from T_{1u}/T_{1p}, θ and k_{uo}/k_{po}, as defined in Equations 7 and 4, respectively, in the main text; (F) Estimates of tumour k_{uo} and k_{po} calculated from these equations, which use estimates of T_1s and θ from arterial blood in the chamber. In (A-F), data points represent individual tumours; bars represent mean ± SEM; $n = 9$; * represents a significant difference between groups; $p = 0.047$ and $p = 0.285$ for (E) and (F), respectively (two-tailed paired t-test)

3.6 | Influence of physiological status on K_{ip} and K_{iu} estimated from the general model

General anaesthesia is a well-known cardiovascular and respiratory depressant and, as such, is likely to influence the estimated values of K_i. Figure 7B shows MABP and the respiration rate measured shortly after arterial cannula implant (experiment 0 in Figure 7B) to the end of the experimental procedures. Both parameters were depressed from normal unanaesthetised values, as expected, and tended to reduce with time, although stabilising towards the end of the procedure. MABP was 72 ± 4 mmHg at the start of the experiment (Figure 7B), which was somewhat lower than we have previously measured in the same animal strain, with propofol[26] or Hypnorm/Hypnovel anaesthesia,[28] as opposed to the isoflurane anaesthesia used here. Consistent with a depressed respiration rate, average arterial oxygen partial pressure (pO$_2$), calculated over the whole experimental time-course, measured 64 ± 3 mmHg, down from the normal range of 80–100 mmHg. The arterial partial pressure of CO$_2$ and arterial pH (42 ± 0.8 mmHg and 7.4 ± 0.03, respectively) were within the normal ranges.

Because blood flow to experimental tumours is highly sensitive to changes in arterial blood pressure,[17–19] the relationships between K_{ip} and K_{iu} and MABP were investigated to determine whether variable MABP between animals could explain the interanimal variability in K_{ip} and K_{iu}. The results are shown in Figure 7C. The correlation was marginal, with statistical significance reached for urea ($p = 0.025$), but not for pyruvate ($p = 0.11$). There was no significant correlation between K_is and tumour size (as estimated from caliper measurements), which was the expected result for the tumour size range used[29] (data not shown).

3.7 | Estimates of k_{pl} and $k_{loss(lactate)}$ in tumour tissue using the precursor-product models

Figure 8A shows an example of tumour signal time-courses for pyruvate and lactate from experiment 1 (TR = 1 s). The raw pyruvate signal (black crosses in Figure 8A) was used as the input for the lactate signal. Using the original precursor-product model without a waiting room compartment, k_{pl} was estimated as 0.049 ± 0.006 s^{-1}, which is exactly the same as for the general model, providing a useful cross-check.

When a waiting room compartment was added to the model to account for the delay in arrival of the tumour lactate signal, it follows that the estimate of k_{pl} would increase, although the increase did not reach statistical significance in this case (0.069 ± 0.014 vs. 0.049 ± 0.006 s^{-1};
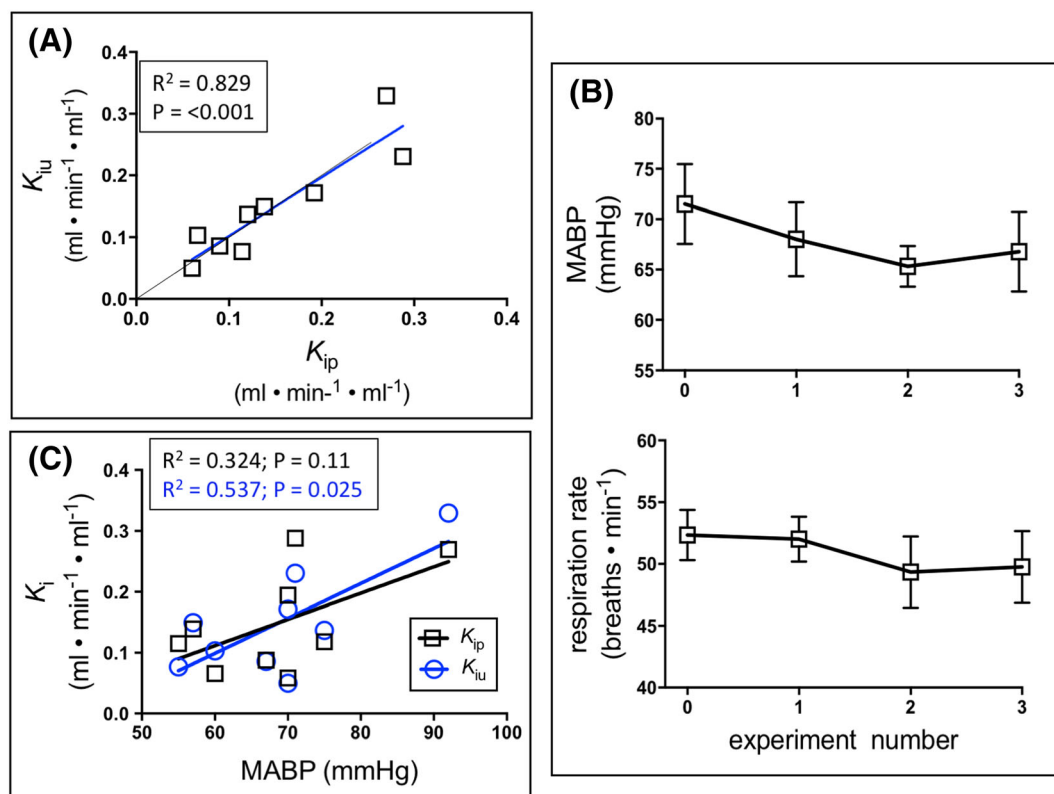
FIGURE 7 Analysis of pyruvate and urea delivery to tumours. (A) Correlation between the clearance rates of urea (K_{iu}) and pyruvate (K_{ip}) from blood to tumour tissue; the blue line is the line of best fit by linear regression; the black line is the line of equivalence; each point represents an individual tumour; n = 9. (B) Variation in mean arterial blood pressure (MABP) and respiration rate of animals throughout the time-course of experiments 1 to 3; data at 0 on the horizontal axis are taken immediately after completion of the cannulation procedure, as described in the main text; each point represents mean ± SEM; n = 9. (C) Correlation between K_{ip} and K_{iu} and MABP for experiment 1; the solid lines are the lines of best fit by linear regression; black symbols are pyruvate; blue symbols are urea; each point represents an individual animal; n = 9

$p = 0.064$). The fractional rate constant k_{avail} describes the turnover of the waiting room compartment (see Appendix C). Figure 8B shows that k_{avail} was highly variable between animals and, for k_{avail} more than approximately 1.0 s^{-1} (i.e., complete turnover of the compartment in 1 s or less), estimates of k_{pl} were independent of whether the original or waiting room precursor-product model was used. Furthermore, there was an inverse relationship between k_{pl} estimated from the waiting room model and k_{avail}. This suggests that a constant absolute rate of pyruvate-lactate exchange could be maintained by a faster turnover of the available labelled pyruvate pool, when pyruvate is retained in the 'waiting room' for a considerable time. As expected, the additional waiting room compartment made no difference to the estimate of $k_{loss(lactate)}$ (0.048 ± 0.003 vs. 0.049 ± 0.003 s^{-1} in each case; $p = 0.609$).

Figure 8C shows the effect of shortening TR on estimates of $k_{loss(lactate)}$ in tumour tissue. There was no statistically significant difference in the values across all three TRs ($p = 0.481$; ANOVA with repeated measures), but there was a statistically significant difference between the data at TR = 1 and 4 s ($p = 0.044$; Tukey's multiple comparison post-test). The calculated tumour θ was 7.2 ± 0.7 degrees, which compares with 9.7 ± 0.9 degrees estimated from the arterial blood data (Figure 4). The lower limit estimate of T_{1l} in tumour tissue was 24.3 ± 2.2 s, which compares with 16.6 ± 1.2 s for T_{1p} estimated from the arterial blood data (Figure 4). Similarly, the lower limit estimate of T_{1u} in tumour tissue was 14.0 ± 1.3 compared with 10.4 ± 1.2 s for arterial blood (Figure 4). The effects of arterial blood versus tumour tissue θ and T_1 estimates on tumour parameter estimates derived from the general model are illustrated in Table 1. The data show that varying T_1 and θ had a small but significant effect on K_is, but no significant effect on the other parameters, with k_{pl} shown to be particularly robust, as predicted from the model equations.

4 | DISCUSSION

The upregulation of the glycolytic pathway in tumours is being actively investigated as a target for therapy.[30] In this study, we have refined and extended the experimental and analytical methods previously published[12] for studying pyruvate metabolism in tumour tissue using dDNP and
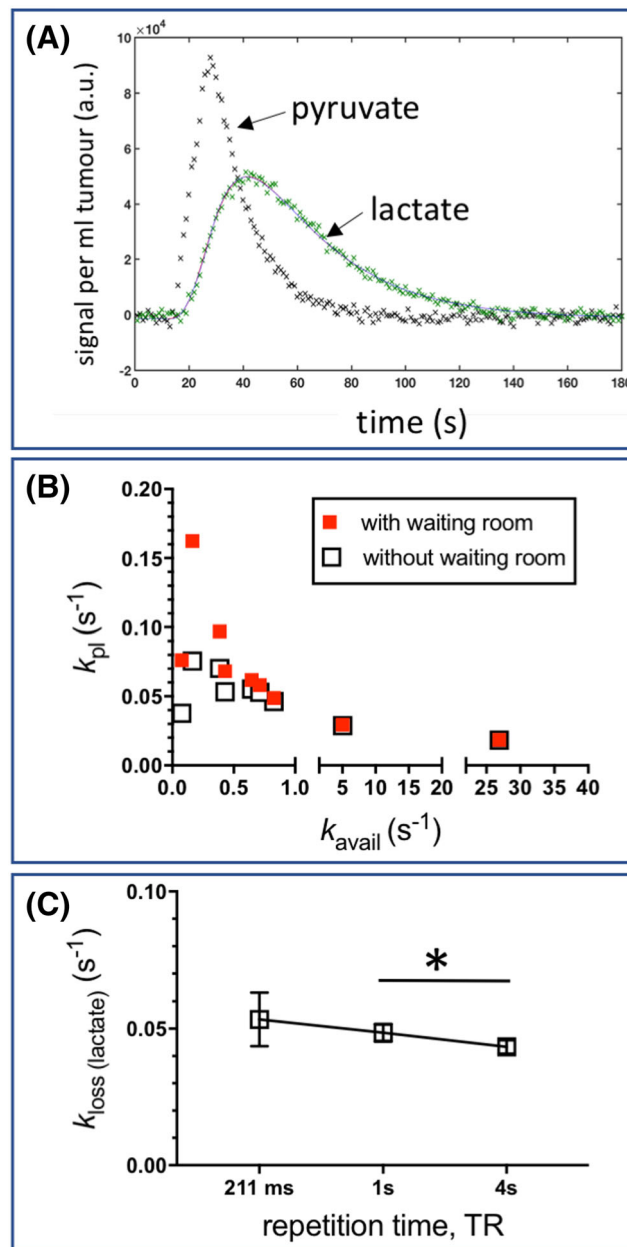
FIGURE 8 Analysis of tumour data using the precursor-product models. (A) An example of tumour pyruvate and lactate signal time-courses in arbitrary units (a.u.) from experiment 1 (TR = 1 s), in the same individual animal as shown in Figures 3 to 5; data points are shown as crosses; the line through the lactate data is derived from the convolution of the pyruvate and lactate time-courses, using the raw pyruvate date as input for the lactate; (B) k_{pl} versus k_{avail}, where k_{avail} is the fractional rate constant for transfer of pyruvate signal from the nonexchanging to exchanging tumour compartment in the 'waiting room' model (Figure 2D). k_{pl} is estimated with a waiting room compartment (solid red symbols) or without (open black symbols); each tumour is represented by a red and an open symbol; n = 9; (C) Variation of $k_{loss(lactate)}$ with variation in TR, using the raw pyruvate data as input for lactate; symbols are mean ± SEM for n = 9; model 2b in Figure 2 was used for the deconvolutions; * represents a significant difference between groups, $p = 0.044$ (Tukey's multiple comparisons test)

compared parameter estimates for its tumour uptake and efflux with that of urea, a nonmetabolised marker. Our findings help to clarify the fate of pyruvate in tumour tissue and the utility of urea as a perfusion marker for dDNP experiments.

4.1 | General model: delivery

A general model incorporating an AIF provides a full picture of pyruvate fate in tumour tissue, from delivery to efflux. Although a gamma-variate function gave a good fit for defining AIFs as used previously,[12] a spectral fitting method, introduced here, proved superior and was used for the

TABLE 1 Comparison of T_1 and θ estimates derived from arterial blood and tumour tissue and their effects on tumour tissue parameter estimates using the general model

	T_1s and θ derived from arterial blood		T_1s and θ derived from tumour tissue		
	mean	SEM	mean	SEM	p value (paired t-test)
$T_{1p/l}$ (s)	16.6	1.2	24.31[a]	2.2	0.015*
T_{1u} (s)	10.4	1.2	14.01[a]	1.3	0.06
θ (degrees)	9.7	0.9	7.2	0.7	0.046*
K_{ip} (ml.min^{-1}.ml^{-1})	0.149	0.028	0.194	0.042	0.021*
k_{pl} (s^{-1})	0.049	0.006	0.05	0.006	0.699
k_{lp} (s^{-1})	−0.003	0.003	−0.005	0.005	0.221
R_p (s^{-1})	0.057	0.008	0.047	0.013	0.194
R_l (s^{-1})	0.053	0.008	0.056	0.009	0.215
K_{iu} (ml.min^{-1}.ml^{-1})	0.148	0.029	0.206	0.04	0.003*
R_u (s^{-1})	0.083	0.017	0.119	0.06	0.436

[a]lower limits on the estimates.
*statistically significant difference at the 5% level.
data are for n = 9 subjects.

main results. A similar model for ^{13}C-urea enabled a direct comparison to be made of the fate of pyruvate and urea in tumour tissue, the latter having been used previously as a blood perfusion marker in dDNP experiments.[7,31,32]

In mammals, urea is an end product of amino acid metabolism, with further catabolism performed by bacteria in the gut.[33] It is a small but highly polar molecule with low lipid solubility. Nevertheless, it is often described as freely diffusible through lipid bilayers, its transport being facilitated by molecular transporters. UT-B urea transporters are found in many nonrenal cells and all endothelial cells studied so far, including capillary endothelial cells.[34,35] Although some authors have assumed that intravenously administered urea remains in the vasculature of tumours, at least for the short observation period available for dDNP,[32] others have shown it readily entering the interstitium.[36] In a dDNP study, the apparent diffusion coefficient for ^{13}C-urea was estimated to be very similar to that of water, also implying rapid clearance of urea from the blood to the interstitium.[37] Our study has confirmed that urea is rapidly cleared from blood into tumour tissue and, furthermore, that the rate of urea clearance (K_{iu}) is equivalent to that of pyruvate (K_{ip}).

Because $K_i = E \times F$ and pyruvate and urea were administered simultaneously, our results indicate that permeability of the tumour vasculature to the two solutes, and not only their K_is, were equivalent. The absolute estimates of K_is were variable between animals, indicating intertumour variability in vascular function. The estimates were also somewhat lower than the expected blood flow rate of the P22 tumour, previously estimated to be around 0.4 ml of blood per min per g of tumour, for MABP 80–90 mmHg.[19,38,39] A reduced driving pressure for tumour blood flow, arising from the relatively low arterial blood pressures measured here, could explain the low K_is obtained. Indeed, a statistically significant direct correlation between K_{iu} and MABP was found, although a tendency for K_{ip} to correlate with MABP did not reach statistical significance. A larger subject group would be needed to determine this relationship for sure. All the K_i values were less than the expected 0.4 ml.min^{-1}.ml^{-1} for F, even at the higher end of the MABP range, suggesting that the uptakes of both pyruvate and urea into tumour tissue are somewhat permeability limited (E < 1.0), making neither an ideal blood flow marker. This would require direct investigation but, in any case, the equivalence of K_is for pyruvate and urea suggests that the inclusion of urea in dDNP experiments has no real benefit for providing information on blood flow over and above what can be obtained from pyruvate alone.

Notably, our estimates of K_{iu} were roughly an order of magnitude lower than those for the similar parameter, K_{trans} for urea, previously published by Chen et al.[7] in transgenic prostate tumours. Together with a blood flow rate of 0.6 ml.min^{-1}.ml^{-1} for this tumour type,[40] this would yield a value for E well above 1.0, which is impossible, indicating that the estimate of K_{trans} was unrealistically high. Inaccuracies in parameter estimates are a major problem in MRS/MRI,[41] with efforts being made to overcome such obstacles in order to progress full translation of hyperpolarisation techniques to the clinic.[8] It is worth noting that the term 'perfusion' has been used by different investigators to refer to different phenomena in tumours. Bahrami et al.[32] used perfusion to refer to the total amount of pyruvate or urea in tissue, and so as not to be confused with blood flow rate, F, or the blood clearance term K_i is used here.

4.2 | General model: metabolism and losses

Assuming that the reactions catalysed by lactate dehydrogenase (LDH) are at or close to chemical equilibrium, the ^{13}C-dDNP experiments are primarily measuring label exchange between pyruvate and lactate, rather than net production of lactate.[42] Thus, the negligible estimate of k_{lp} is

consistent with the LDH reaction lying heavily towards lactate and a relatively large lactate pool in the P22 tumour.[26] The estimate of k_{pl} obtained here was very similar to those obtained previously in the P22 tumour.[12,26]

We detected no ^{13}C-labelled lactate signal in arterial blood as reported previously in rats[12] and by others in mice,[14] although a small signal was observed by Marjanska et al., using a coil directly surrounding the carotid artery in rats.[23] Blood lactate concentration is normally in the low mM range but higher in tumour-bearing mice[14] and in some cancer patients.[13] Serrao et al.[14] found evidence for export of ^{13}C-labelled lactate from the intracellular to the extracellular space of tumours in dDNP experiments in vivo, consistent with tumour-promoting effects of lactate occurring between different cell populations within the tumour microenvironment.[9,10] They also found a significant concentration of ^{13}C-labelled lactate (2.4 μmol/g) in mixed venous and arterial blood 30 s after intravenous administration of ^{13}C-labelled pyruvate, as measured from perchloric acid extracts, approximately 50% of which could be attributed to lactate release from tissues other than blood. Taken together, these results point to a marked efflux of lactate from tumour tissue into venous blood, which is generally not detectable by [13]C_1-pyruvate-based dDNP experiments. Indeed, recent evidence suggests that lactate produced by tumours is exchanged extremely rapidly with the circulation and that circulating lactate is a primary substrate for the TCA cycle in most tissues and tumours.[43,44] Unfortunately, our estimates of the fractional rate constant for lactate efflux from tumour into blood (k_{lo}) and the equivalent parameters for pyruvate and urea (k_{po} and k_{uo}) were negative. Accurate estimates of efflux parameters would enable calculation of tumour distribution volumes for these solutes. Others have calculated the distribution volumes, denoted V_T, of hyperpolarised urea and butanol, in transgenic prostate tumours in mice.[40] Especially notable was the surprisingly low V_T for butanol (0.25 ± 0.19), which is lipid soluble and readily diffusible in tissue, with the V_T for urea even lower (0.10 ± 0.07). However, as for our results, these estimates were found to be highly dependent on the assumed values for T_1 and so are likely to be inaccurate.

4.3 | Precursor-product model

The precursor-product model provides a relatively straightforward approach to estimating k_{pl} in tumours via dDNP and is the most practical approach, if this is the only parameter of interest and there is no detectable lactate input from blood. In addition, repeat experiments in which TR was varied enabled estimates of θ and a lower limit on T_{1l} for tumour tissue to be obtained, which clearly showed that estimates of these parameters in arterial blood were poor surrogates for the tumour tissue. Although T_1 is mainly governed by interactions between the ^{13}C-nucleus and protons, it is well known that T_1 can be modified by other environmental factors. Oxygenation differences between arterial blood and tumour tissue could partially account for the observed differences in T_1 estimates. Although we did not detect signal from lactate in blood, we cannot exclude the possibility that pyruvate metabolism in fresh arterial blood also shortened the blood T_{1p} via a combination of oxidative metabolism in leucocytes and low level production of lactate in leucocytes and/or erythrocytes. Recent advances in mapping T_1s for hyperpolarised probes in living tissue have been made using balanced steady state free precession acquisitions,[45] but estimates are still compromised to some extent by blood flow and are difficult to apply to rapidly metabolised probes with short T_1 products or closely spaced frequencies. In future experiments, use of a volume transmitting coil, in combination with a surface receiving coil, would reduce uncertainty issues with θ and aid T_1 estimations. In addition, a single experiment incorporating both short and long TRs to estimate T_1s and θ, as used by Puckeridge et al.,[46] would reduce scanning time, and the use of a B1-insensitive adiabatic pulse, such as BIR, would improve B1 homogeneity and flip angle consistency for use with a surface coil. In any event, although k_{pl} is a very robust parameter, and the clearance parameters K_{ip} and K_{iu} estimated from the general model were only moderately T_1-dependent (Table 1), much more accurate estimates of tumour T_1 are required before solute effluxes can be investigated reliably. In addition, it should be noted that calculation of the efflux fractional rate constants k_{po}, k_{lo} and k_{uo} are also dependent on estimates of the lumped loss parameters R_p, R_l and R_u, respectively (Equations (4, 5 and 7)), and so we cannot discount the possibility that underestimation of these parameters (from the general model analysis) could also have contributed to the negative efflux parameter values obtained.

The accuracy of k_{pl} estimates was improved by addition of a 'waiting room' compartment to the precursor-product model. Bankson et al.,[11] using Akaike's criterion, found that inclusion of two spatial compartments (intravascular and extravascular/extracellular), in addition to two chemical compartments (pyruvate and lactate), in their modelling, provided a good balance between accuracy of parameter estimation and complexity compared with having a single spatial compartment in which pyruvate is immediately available for chemical exchange. Furthermore, extending the model to include three spatial compartments (intravascular, extracellular and intracellular), although a more accurate description of the biology, provided no further statistical advantage under the conditions of their experiments. Our waiting room model is also made up of two spatial compartments in the tumour, although the biological significance of the waiting room is unclear. It most likely reflects the complexities of the tumour microcirculation, in which blood flow rate is highly heterogeneous,[38] and filling of the whole vascular bed with contrast agent entering through supplying arterioles can take several seconds.[47] The fractional rate constant, k_{avail}, describing the kinetics of pyruvate transfer from the waiting room compartment to the exchangeable pyruvate compartment, was highly variable between animals, suggesting that there was considerable intertumour, in addition to intratumour, heterogeneity in vascular function, which is consistent with the estimates of K_{ip} obtained from the general model. k_{pl} estimates from the waiting room model were inversely related to k_{avail}, suggesting that the absolute rate of pyruvate-lactate exchange could be maintained over the whole k_{avail} range. However, without knowing the concentrations of pyruvate in each compartment, this cannot be known for certain. In future studies, it would be worth determining whether k_{avail} is a useful descriptor of tumour vascular function. Others have suggested that pyruvate flux into cells through monocarboxylate transporter 1 (MCT-1)[48] and/or its efflux from cells via MCT-4[49] could also

influence appearance of the lactate signal. Our model cannot discriminate between these different processes, but the waiting room model does provide a more reliable estimate of k_{pl} based on a better description of the biological processes involved in pyruvate-lactate exchange than simpler models with only one spatial compartment.

5 | CONCLUSION

The precursor-product model is straightforwardly applied to tumour $^{13}C_1$-pyruvic acid dDNP data and so has obvious clinical utility, primarily for estimating k_{pl}. This model is improved by the incorporation of a nonexchanging spatial compartment to account for the delay in appearance of the lactate signal compared with the pyruvate signal in tumour tissue. We have demonstrated some of the further information that can be gained from modelling the full process in preclinical tumour models, from pyruvate delivery to its metabolism and efflux back into the blood. The modelling revealed that the P22 tumour vasculature is as permeable to urea as pyruvate, suggesting that use of urea provides no additional information on the tumour microcirculation over and above what can be obtained from pyruvate alone. The study also highlights the need for rigorous processes controlling signal quantitation and accurate estimation of signal decay in tumour tissue, if absolute estimations of biological parameters are required.

ENDNOTE

* Note that throughout the text k represents a fractional rate constant in s^{-1}, whereas K represents a rate in defined units, as described in the main text. Subscripts i and o refer to movement of pyruvate/lactate/urea in and out of tumour tissue, respectively; subscripts p, l and u refer to pyruvate, lactate and urea, respectively.

DATA AVAILABILITY STATEMENT

The data that support the findings of this study are available from the corresponding author upon reasonable request.

ORCID

Steven Reynolds https://orcid.org/0000-0002-6463-8471

Samira M. Kazan https://orcid.org/0000-0001-8404-7727

Adriana Anton https://orcid.org/0000-0002-1356-4513

Tooba Alizadeh https://orcid.org/0000-0002-3193-6050

Martyn N. Paley https://orcid.org/0000-0002-9710-8573

Gillian M. Tozer https://orcid.org/0000-0003-2581-3019

REFERENCES

1. Ardenkjaer-Larsen JH, Fridlund B, Gram A, et al. Increase in signal-to-noise ratio of > 10,000 times in liquid-state NMR. *Proc Natl Acad Sci USA*. 2003; 100:10158-10163.
2. Golman K, Zandt RI, Lerche M, Pehrson R, Ardenkjaer-Larsen JH. Metabolic imaging by hyperpolarized 13C magnetic resonance imaging for in vivo tumor diagnosis. *Cancer Res*. 2006;66:10855-10860.
3. Day SE, Kettunen MI, Gallagher FA, et al. Detecting tumor response to treatment using hyperpolarized 13C magnetic resonance imaging and spectroscopy. *Nat Med*. 2007;13:1382-1387.
4. Nelson SJ, Kurhanewicz J, Vigneron DB, et al. Metabolic imaging of patients with prostate cancer using hyperpolarized [1-(1)(3)C]pyruvate. *Sci Transl Med*. 2013;5:198ra108.
5. Park I, Larson PEZ, Gordon JW, et al. Development of methods and feasibility of using hyperpolarized carbon-13 imaging data for evaluating brain metabolism in patient studies. *Magn Reson Med*. 2018;80:864-873.
6. Gallagher FA, Woitek R, McLean MA, et al. Imaging breast cancer using hyperpolarized carbon-13 MRI. *Proc Natl Acad Sci USA*. 2020;117:2092-2098.
7. Chen HY, Larson PEZ, Bok RA, et al. Assessing prostate cancer aggressiveness with hyperpolarized dual-agent 3D dynamic imaging of metabolism and perfusion. *Cancer Res*. 2017;77:3207-3216.
8. Kurhanewicz J, Vigneron DB, Ardenkjaer-Larsen JH, et al. Hyperpolarized (13)C MRI: path to clinical translation in oncology. *Neoplasia*. 2019;21:1-16.
9. Dhup S, Dadhich RK, Porporato PE, Sonveaux P. Multiple biological activities of lactic acid in cancer: influences on tumor growth, angiogenesis and metastasis. *Curr Pharm Des*. 2012;18:1319-1330.

10. de la Cruz-Lopez KG, Castro-Munoz LJ, Reyes-Hernandez DO, Garcia-Carranca A, Manzo-Merino J. Lactate in the regulation of tumor microenvironment and therapeutic approaches. *Front Oncol*. 2019;9:1143.

11. Bankson JA, Walker CM, Ramirez MS, et al. Kinetic modeling and constrained reconstruction of hyperpolarized [1-13C]-pyruvate offers improved metabolic imaging of tumors. *Cancer Res*. 2015;75:4708-4717.

12. Kazan SM, Reynolds S, Kennerley A, et al. Kinetic modeling of hyperpolarized (13)C pyruvate metabolism in tumors using a measured arterial input function. *Magn Reson Med*. 2013;70:943-953.

13. Fischer K, Hoffmann P, Voelkl S, et al. Inhibitory effect of tumor cell-derived lactic acid on human T cells. *Blood*. 2007;109:3812-3819.

14. Serrao EM, Kettunen MI, Rodrigues TB, et al. Analysis of (13) C and (14) C labeling in pyruvate and lactate in tumor and blood of lymphoma-bearing mice injected with (13) C- and (14) C-labeled pyruvate. *NMR Biomed*. 2018;31:e3901.

15. Khegai O, Schulte RF, Janich MA, et al. Apparent rate constant mapping using hyperpolarized [1-(13)C]pyruvate. *NMR Biomed*. 2014;27:1256-1265.

16. Larson PEZ, Chen HY, Gordon JW, et al. Investigation of analysis methods for hyperpolarized 13C-pyruvate metabolic MRI in prostate cancer patients. *NMR Biomed*. 2018;31:e3997.

17. Vaupel P. Interrelationship between mean arterial blood pressure, blood flow and vascular resistance in solid tumor tissue of DS-carcinosarcoma. *Exp Dermatol*. 1975;31:587-589.

18. Sensky PL, Prise VE, Tozer GM, Shaffi KM, Hirst DG. Resistance to flow through tissue-isolated tumours located in two different sites. *Br J Cancer*. 1993;67:1337-1341.

19. Tozer GM, Shaffi KM. Modification of tumour blood flow using the hypertensive agent, angiotensin II. *Br J Cancer*. 1993;67:981-988.

20. Workman P, Aboagye EO, Balkwill F, et al. Guidelines for the welfare and use of animals in cancer research. *Br J Cancer*. 2010;102:1555-1577.

21. Reynolds S, Kazan SM, Bluff J, et al. Fully MR compatible syringe pump for the controllable injection of hyperpolarised substrate in animals. *Appl Magn Reson*. 2012;43:263-273.

22. Lau JY, Chen AP, Gu YP, Cunningham CH. A calibration-based approach to real-time in vivo monitoring of pyruvate C(1) and C(2) polarization using the JCC spectral asymmetry. *NMR Biomed*. 2013;26:1233-1241.

23. Marjanska M, Teisseyre T, Halpern-Manners N, et al. Measurement of arterial input function in hyperpolarized 13C studies. *Appl Magn Reson*. 2012;43:289-297.

24. Cunningham VJ, Jones T. Spectral analysis of dynamic PET studies. *J Cereb Blood Flow Metab*. 1993;13:15-23.

25. Nelder JA, Mead R. A simplex method for function minimisation. *Comput J*. 1965;7:308-313.

26. Bluff JE, Reynolds S, Metcalf S, et al. Measurement of the acute metabolic response to hypoxia in rat tumours in vivo using magnetic resonance spectroscopy and hyperpolarised pyruvate. *Radiother Oncol*. 2015;116:392-399.

27. Sourbron SP, Buckley DL. Tracer kinetic modelling in MRI: estimating perfusion and capillary permeability. *Phys Med Biol*. 2012;57:R1-R33.

28. Tozer GM, Shaffi KM. The response of tumour vasculature to angiotensin II revealed by its systemic and local administration to "tissue-isolated" tumours. *Br J Cancer*. 1995;72:595-600.

29. Tozer GM, Sensky PL, Shaffi KM, Prise VE, Cunningham VJ. Characterisation of the microcirculation of tumours where the blood supply originates from a single artery and vein. *Adv Exp Med Biol*. 1994;345:367-374.

30. Muthu M, Nordstrom A. Current status and future prospects of clinically exploiting cancer-specific metabolism - Why is tumor metabolism not more extensively translated into clinical targets and biomarkers? *Int J Mol Sci*. 2019;20:1385.

31. von Morze C, Larson PE, Hu S, et al. Investigating tumor perfusion and metabolism using multiple hyperpolarized (13)C compounds: HP001, pyruvate and urea. *Magn Reson Imaging*. 2012;30:305-311.

32. Bahrami N, Swisher CL, Von Morze C, Vigneron DB, Larson PE. Kinetic and perfusion modeling of hyperpolarized (13)C pyruvate and urea in cancer with arbitrary RF flip angles. *Quant Imaging Med Surg*. 2014;4:24-32.

33. Levenson SM, Crowley LV, Horowitz RE, Malm OJ. The metabolism of carbon-labeled urea in the germ free rat. *J Biol Chem*. 1959;234:2061-2062.

34. Sands JM. Molecular mechanisms of urea transport. *J Membr Biol*. 2003;191:149-163.

35. Yu L, Liu T, Fu S, et al. Physiological functions of urea transporter B. *Pflugers Arch*. 2019;471:1359-1368.

36. Ettinger SN, Poellmann CC, Wisniewski NA, et al. Urea as a recovery marker for quantitative assessment of tumor interstitial solutes with microdialysis. *Cancer Res*. 2001;61:7964-7970.

37. Patrick PS, Kettunen MI, Tee SS, et al. Detection of transgene expression using hyperpolarized 13C urea and diffusion-weighted magnetic resonance spectroscopy. *Magn Reson Med*. 2015;73:1401-1406.

38. Tozer GM, Shaffi KM, Prise VE, Bell KM. Spatial heterogeneity of tumour blood flow modification induced by angiotensin II: relationship to receptor distribution. *Int J Cancer*. 1996;65:658-663.

39. Tozer GM, Prise VE, Lewis G, Xie S, Wilson I, Hill SA. Nitric oxide synthase inhibition enhances the tumor vascular-damaging effects of combretastatin a-4 3-o-phosphate at clinically relevant doses. *Clin Cancer Res*. 2009;15:3781-3790.

40. von Morze C, Bok RA, Reed GD, Ardenkjaer-Larsen JH, Kurhanewicz J, Vigneron DB. Simultaneous multiagent hyperpolarized (13)C perfusion imaging. *Magn Reson Med*. 2014;72:1599-1609.

41. Ng CS, Wei W, Bankson JA, et al. Dependence of DCE-MRI biomarker values on analysis algorithm. *PLoS ONE*. 2015;10:e0130168.

42. Kettunen MI, Hu DE, Witney TH, et al. Magnetization transfer measurements of exchange between hyperpolarized [1-13C]pyruvate and [1-13C]lactate in a murine lymphoma. *Magn Reson Med*. 2010;63:872-880.

43. Hui S, Ghergurovich JM, Morscher RJ, et al. Glucose feeds the TCA cycle via circulating lactate. *Nature*. 2017;551:115-118.

44. Garcia-Canaveras JC, Chen L, Rabinowitz JD. The tumor metabolic microenvironment: lessons from lactate. *Cancer Res*. 2019;79:3155-3162.

45. Milshteyn E, Reed GD, Gordon JW, et al. Simultaneous T1 and T2 mapping of hyperpolarized (13)C compounds using the bSSFP sequence. *J Magn Reson*. 2020;312:106691.

46. Puckeridge M, Pages G, Kuchel PW. Simultaneous estimation of T(1) and the flip angle in hyperpolarized NMR experiments using acquisition at non-regular time intervals. *J Magn Reson*. 2012;222:68-73.

47. Brurberg KG, Gaustad JV, Mollatt CS, Rofstad EK. Temporal heterogeneity in blood supply in human tumor xenografts. *Neoplasia*. 2008;10:727-735.

48. Harris T, Eliyahu G, Frydman L, Degani H. Kinetics of hyperpolarized 13C1-pyruvate transport and metabolism in living human breast cancer cells. *Proc Natl Acad Sci USA*. 2009;106:18131-18136.

49. Sriram R, Van Criekinge M, Hansen A, et al. Real-time measurement of hyperpolarized lactate production and efflux as a biomarker of tumor aggressiveness in an MR compatible 3D cell culture bioreactor. *NMR Biomed.* 2015;28:1141-1149.

50. Lawson C, Hanson R. *Solving least squares problems.* Hoboken, NJ: Prentice-Hall; 1974.

APPENDIX A: Simultaneous fits to blood data

To measure the flip angle, θ, in blood, a dataset with a rapid RF excitation pulse train (TR = 0.211 s; experiment 3; pyruvate only) was used to erode the magnetization, so that the term $e^{-\frac{n\,TR}{T1}}$ in Equation 1 tended towards 1. This data was then least squares fitted to $M(t,n) = M_0 (cos\theta)^n$ to obtain an initial estimate of the flip angle (θ) in blood. The next step was to fit pyruvate data obtained from blood with a longer TR = 4 s (experiment 2), using the initial estimate of the θ already calculated, using Equation 1, to provide an initial estimate of T_{1p} in blood. Following this, the urea time series with the same TR = 4 s was fit to Equation 1, using the estimate of θ already obtained from the pyruvate data, to calculate an initial estimate of T_{1u}. Finally, the time-courses for signal from blood for both pyruvate and urea were least squares fit simultaneously, solving for θ, T_{1p} and T_{1u} using the values already calculated above as initial estimates of these parameters.

APPENDIX B: Spectral analysis method for deriving the AIF

The spectral analysis method, previously used in positron emission tomography tracer studies,[24] was used to derive the tumour AIFs for pyruvate and urea.

The AIF is described as the convolution of a square wave (to describe the shape of the venous infusion schedule of hyperpolarised pyruvate/ urea), with a positive sum of kinetic exponential basis functions (to provide an unconstrained fit of the data) and is given by:

$$AIF(t) = \Sigma_{j=1,N}\ S(t) \bigotimes \alpha_j \exp\left(-\beta_j t\right). \tag{A2.1}$$

The measured signal time-course in the chamber (AIF$_{meas}$) is a convolution of AIF with a single exponential for dispersion, accounting for the mixing of the blood in the chamber:

$$AIF_{meas}(t) = AIF(t) \bigotimes K1 \exp\left(-kt\right), \tag{A2.2}$$

where $\bigotimes$ denotes the convolution operator; S(t) is the square wave; N is the total number of basis functions included in the fitting process (N = 100); $K1$ is the flow rate of arterial blood into the chamber in ml s^{-1}; k is the fractional loss of signal from the chamber due to relaxation losses (T_1 and θ) and the turnover of blood in the chamber ($K1$ divided by the chamber volume).

Thus, the problem becomes one of determining the values of α that best fit the measured data given a set of N predefined β values. The β values cover a full spectrum of feasible kinetics ranging from $\beta = 0.0001$ s^{-1} to the fastest measurable dynamic, $\beta = 1$ s^{-1} (subject to the constraint $\alpha > 0$). The positivity constraint for α resolves the problem of finding a solution to an underdetermined set of equations and imposes a sparse solution on the spectral part of the fitting process and is solved using a non-negative least squares algorithm.[24,50]

This whole process corresponds to fitting Equation A2.2 to the measured blood chamber data and enables estimation of AIF(t), which is equivalent to C_P and C_U for pyruvate and urea, respectively, in Figure 2.

APPENDIX C: Precursor-product models

Estimates of k_{pl} (forward fractional rate constant for pyruvate-lactate exchange) and $k_{loss(lactate)}$ (fractional rate constant for total tumour lactate loss) can be obtained without the need for a blood arterial input function using the precursor-product relationship between tumour pyruvate and tumour lactate signal time-courses ($PP(t)$ and $LP(t)$, respectively). Precursor-product models were based on the full general models shown in Figure 2B,D.

A delay of a few seconds was consistently observed between $PP(t)$ and $LP(t)$, suggesting that not all the tumour pyruvate was immediately accessible to the enzyme catalysing its exchange with lactate. As described previously,[12] this can be modelled as a simple delay, which is then used as a fixed value in the subsequent modelling. The delay length, d, was determined by iteratively fitting the signal over a range of values for d from 0 to 10 s and selecting the value with the smallest residual sum of squares. k_{pl} and $k_{loss(lactate)}$ were derived from the differential Equation 3 in the main text:

$$\frac{dLP}{dt} = k_{pl}PP(t) - (R_l + k_{lp})LP(t)$$

with the solution:

$$LP(t) = PP(t) \bigotimes k_{pl}.\exp\left(-\left(k_{loss(lactate)}\right)t\right), \tag{A3.1}$$

where $k_{loss(lactate)} = R_l + k_{lp}$ and Equation A3.1 describes the precursor-product model based on Figure 2B. The final lactate concentration was calculated by accounting for the delay in the lactate signal by time shifting it by a duration of d and using the associated decay constant, $dc = \exp(-d^*[kT_1 + k\theta])$, to correct for the loss of signal in this time, where $kT_1 = 1/T_1$ and $k\theta = (1 - cos\theta)/TR$. In experiment 3, due to the very short TR, the signal time-courses were only measured after the peak in tissue signal occurred and so it was necessary to include a starting value for the tissue lactate fit.

However, the observed delay between tumour lactate and pyruvate signals most likely reflects turnover of pyruvate in an additional 'waiting room' tumour tissue compartment, as shown in Figure 2D and described by:

$$\frac{dLP}{dt} = k_{pl}PE(t) - (R_l + k_{lp})LP(t)$$

$$\frac{dPE}{dt} = k_{avail}PP(t) - (R_P + k_{avail} + kT1 + k\theta)PE(t),$$

where $PE(t)$ is the concentration of pyruvate in the exchangeable compartment. Solution of these equations yields:

$$LP(t) = PP(t) \bigotimes k_{pl}.\exp\left(-k_{loss(lactate)}\ t\right) \bigotimes k_{avail}.\exp\left(-(k_{pl} + k_{avail} + kT_1 + k\theta)t\right), \tag{A3.2}$$

where k_{avail} is the fractional rate constant for pyruvate turnover in the waiting room compartment.